

Operation of a Microfabricated Planar Ion-trap for Studies of a Yb⁺–Rb Hybrid Quantum System

Abasalt Bahrami^{1,*}, Matthias Müller¹, Martin Drechsler^{1,†}, Jannis Joger², Rene Gerritsma², Ferdinand Schmidt-Kaler¹

¹ QUANTUM, Institut für Physik, Universität Mainz, Staudingerweg 7, 55128 Mainz, Germany

² Van der Waals-Zeeman Institute, Institute of Physics, University of Amsterdam, Science Park 904, 1098 XH Amsterdam, The Netherlands

Key words: Ion trap, Atom trap, Atom-ion interaction

* Corresponding author: e-mail abahrami@uni-mainz.de

† Present address: Departamento de Física, FCEyN, UBA and IFIBA, Conicet, Pabellón 1, Ciudad Universitaria, 1428 Buenos Aires, Argentina.

In order to study interactions of atomic ions with ultracold neutral atoms, it is important to have sub- μm control over positioning ion crystals. Serving for this purpose, we introduce a microfabricated planar ion trap featuring 21 DC electrodes. The ion trap is controlled by a home-made FPGA voltage source providing independently variable voltages to each of the DC electrodes. To assure stable positioning of ion crystals with respect to trapped neutral atoms, we integrate into the overall design a compact mirror magneto optical chip trap (mMOT) for cooling and confining neutral ^{87}Rb atoms. The trapped atoms will be transferred into an also integrated chip-based Ioffe-Pritchard trap potential formed by a Z-shaped wire and an external bias magnetic field. We introduce the hybrid atom-ion chip, the microfabricated planar ion trap and use trapped ion crystals to determine ion lifetimes, trap frequencies, positioning ions and the accuracy of the compensation of micromotion.

Copyright line will be provided by the publisher

1 Introduction The development of laser cooling techniques to cool neutral atoms below μK temperatures and magnetic trapping has paved the way to explore quantum degeneracy in atomic gases [1,2] and to investigate a variety of quantum many-body phenomena [3,4]. On the other hand Paul traps use radio-frequency (RF) driven electric fields and static voltages (DC) to trap ions in a time-averaged trapping potential [5].

Recently, the interactions between neutral atoms and charged ions have been addressed for investigations of low temperature chemical reactions [6,7,8], the study of polaron physics [9], but also to allow for novel types of quantum simulation [10]. From the experimental side, the challenge is to combine both trapping techniques into a hybrid atom-ion trap to study the atom-ion system. At large inter-nuclear separations the collisions between ions and neutral atoms are dominated by an attractive polarization potential of the form

$$V = -\frac{\alpha_p q^2}{(4\pi\epsilon_0)^2 r^4}, \quad (1)$$

where r is the inter-nuclear separation, q the charge of the ion, α_p the isotropic static electric dipole polarizability of the neutral atom and ϵ_0 the vacuum permittivity [11]. In the s-wave scattering limit the characteristic length scale of the interaction of the potential is given by

$$r^* = \sqrt{\frac{\mu\alpha_p q^2}{(4\pi\epsilon_0\hbar)^2}}, \quad (2)$$

where $\mu = m_i m_a / (m_i + m_a)$ is the reduced mass of the two particles involved in the collision and \hbar is the reduced Planck constant [12]. At this separation of the particles the characteristic energy scale $E^* = \hbar^2 / 2\mu R^{*2}$ can be assigned. For the specific case of ^{87}Rb atoms interacting with Yb^+ ions $r^* = 307 \text{ nm}$ [13]. In contrast

Copyright line will be provided by the publisher

Table 1 Possible processes during two-body collisions of a hetero-nuclear ion A^+ with an atom B at low energy. (1) The atom and ion pair may undergo an elastic collision. In case of a perfectly elastic collision the internal states of atom and ion do not change, (2) the pair might exchange spins. (3) An electron from B may hop to A^+ if the particles are close enough to each other. A charge transfer process between B and A^+ may take place in the following ways: radiative charge transfer, photoassociative charge transfer or non-radiative charge transfer. (4) An atom-ion pair in the excited continuum may decay spontaneously to a bound level of lower electronic state.

Types of processes		
(1)	$A^+ + B \rightarrow A^+ + B$	Elastic collisions [11]
(2)	$A^+ \downarrow\rangle + B \uparrow\rangle \rightarrow A^+ \uparrow\rangle + B \downarrow\rangle$	Spin exchange [16, 17]
(3)	$A^+ + B \rightarrow A + B^+$	N-radiative charge transfer
	$A^+ + B \rightarrow A + B^+ + \gamma$	Radiative [18, 19, 20]
	$A^+ + B \rightarrow (AB)^+ + \gamma$	Photoassociative
(4)	$A^+ + B \rightarrow A^+B + \gamma$	Molecule formation [21]

short-range interactions, e.g. for ^{87}Rb atoms, require a wave packet overlap at distances of a few nm [14]. Typical processes emerging from two-body collisions of hetero-nuclear atoms are listed in Tab. 1. Among possible interaction processes, we are interested in processes which are dominated by elastic collisions. The atom-ion scattering cross-section in elastic collisions $\sigma_{el}(E)$ is described by

$$\sigma_{el}(E) = \pi \left(1 + \frac{\pi^2}{16} \right) r^{*2} \left(\frac{\hbar^2}{\mu r^{*2} E} \right)^{1/3}, \quad (3)$$

where $E \approx k_B T_{\text{ion}}$ [15]. To resolve the interactions between the atoms and ions on the length scale of r^* , we need to have a sub- μm accuracy in positioning the ions. In order to position the trapped ions with such accuracy we have to use an ion trap which has enough DC electrodes to confine ions in different trapping regions and position them accurately. For this purpose we use a segmented planar ion trap with 21 DC electrodes which can be independently controlled. By applying DC voltages to each of the opposing DC electrodes ions can be transported all along the trap axis. To investigate the interactions between atoms and ions, we have to spatially overlap the atomic cloud and ion crystals in a single apparatus. A novel atom-ion trap introduced here combines a planar ion trap with an integrated atom trap into a single chip trap. This new chip design implies an infrastructural simplification of the setup featuring an optimal optical access and making the two traps more robust to temporal drifts of the positions of the two species to each other.

Our setup is aiming for studies of the tunneling dynamics of a bosonic Josephson junction coupled to a single or a string of trapped ions (Fig. 1). A single ion trapped in the center of the atomic double-well potential can control the

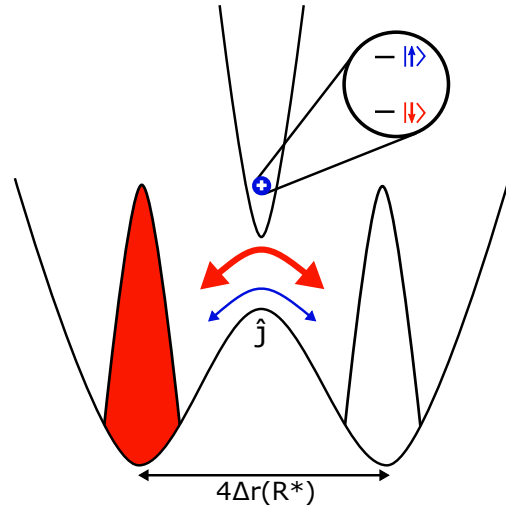


Figure 1 A Bose-Einstein condensate trapped in a double-well potential with an ion in the center. The internal state of the ion is controlled by laser light and controls the tunneling rate \hat{J} .

atomic tunneling rate via spin-dependent atom-ion interactions [22]. Since in this proposal a trapped ion can control many-body tunneling dynamics, mesoscopic entanglement between the atomic matter wave and the spin of the ion may be created. The interplay between the spin-dependent tunneling and the inter-atomic interactions could also result in superposition of quantum self-trapping [23] and Josephson tunneling. Single, neutral impurities have also been proposed as a means to control and measure the dynamics in Josephson junctions, but these typically lack the sub- μm controllability offered by the trapped ion system. We can make tightly confined atomic clouds that have small sizes. This allows to limit the interactions between atoms and ions to the central region of the ion trap, where micromotion induced heating is small [24]. It may also put the 1D regime of atom-ion systems within reach [25], where the trapped ions may induce large effects in the atomic cloud, such as density bubbles [26].

There are several reasons why mixtures of Rb and Yb were selected. i) The excessive micromotion of ion can be minimized by choosing a large ion to atom mass ratio; Yb and Rb atoms are thus a good choice for our experiment [27]. ii) These two species are also thermodynamically favored. Yb $^+$ ions immersed in a Rb atomic cloud can be sympathetically cooled [28]. iii) Yb has seven stable isotopes; including five bosonic and two fermionic species with nuclear spin 1/2 and 5/2 [29] which can be used as a quantum sensor for very weak forces [30]. iv) RbYb ground state molecules have large electric dipole moments, allowing for long range interactions [31]. v) It is easy to implement a mMOT and an Ioffe-Pritchard chip trap for Rb atoms; working with Rb at IR wavelengths does not af-

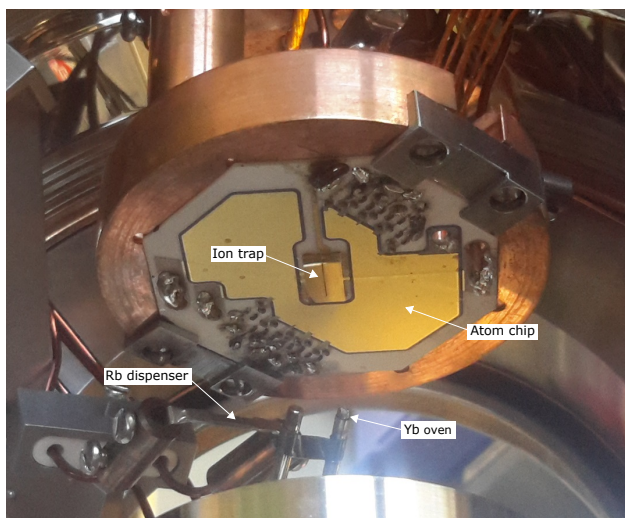


Figure 2 Final assembly of the atom-ion chip with all wire-bonds. The atom source carrier is placed below the trap carrier and it includes a Rb atom dispenser and the Yb atom oven.

fect trapped Yb^+ ions. Rb atoms will be trapped as a spin-polarized sample, thus ideal to follow this proposal [32].

The paper is structured as follows: First, we give an overview of the experimental design, then present the atom trap, the ion trap, its operation with successful trapping of Yb^+ ion crystals and discuss the characterization of the ion trap. Finally we give an outlook of our upcoming experiments. Initial experiments in the hybrid system of interacting ions and atoms have been plagued by micromotion induced heating [27] such that we address this issue specifically in our setup.

2 System overview Our setup consists of a hybrid atom-ion chip trap that can trap laser cooled neutral ^{87}Rb atoms in a mirror-magneto optical trap (mMOT) [33] and transfer them into a tight Ioffe-Pritchard (IP) potential. The IP trap is created by a Z-shaped wire together with a bias magnetic field and we expect trap frequencies of $(\omega_x, \omega_y, \omega_z) = 2\pi \times (1170, 1167, 84)$ Hz from our calculations. Atoms trapped in this IP potential are spatially overlapped with Yb^+ ion crystals which are loaded into a microfabricated planar Paul trap (Fig. 2).

For cooling and trapping of Rb atoms near the surface of the ion trap, we use the chip trap in a mMOT configuration [33]. Rb atom sources are two dispensers (SAES Getters), one implemented behind and one in front of the atom-ion trap (Fig. 2). The atom trap shown in Fig. 3 is fabricated using thick film technology in order to print UHV-compatible, sub-mm-scaled electrical circuits on the Alumina substrate (Al_2O_3). A major benefit of using this technology is the possibility of printing multiple circuit layers separated by isolating layers which we use for our design.

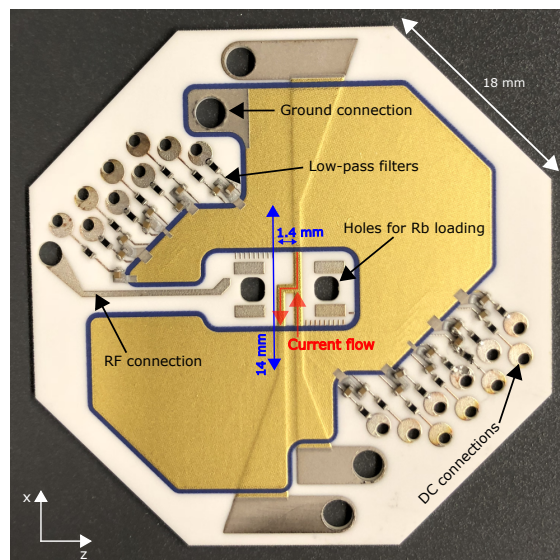


Figure 3 The atom trap is composed of an octagonal chip with an outside diameter of 45 mm which is used as the surface for the atom trap wires, as filter board and as support of the ion trap. This direct mounting assures the required positioning accuracy. In the assembly of atom-ion chip, the ion trap is glued on top of the atom trap covering the central region of the octagon. Electrical bonding wires connect the DC and RF voltage from the octagon to the ion trap chip (Fig. 2). Underneath the octagon chip surface there are a big U-shaped, a small U- and a Z-shaped wire. It is also schematically shown how electric current can flow in the wires during the trapping phase (red arrows) to form the magnetic field configuration required for a mMOT or IP trap. The filter board includes 3.38 MHz low-pass filters ($C = 4.7$ nF, $R = 10$ Ω) on the DC control electrodes to filter RF pickups.

In order to realize a mMOT, we need two σ^+ circular polarized and two σ^- circular polarized laser beams and a quadrupole magnetic field. Our Rb-laser system consists of two home-made external cavity diode lasers (Panasonic LNC728PS01WW) with a maximum output power of 200 mW at continuous wave condition. These lasers are individually frequency stabilized to the atomic transitions in the D2 line of ^{87}Rb ($5^2S_{1/2} \rightarrow 5^2P_{3/2}$) through frequency modulation spectroscopy. The cooling laser frequency is locked to the crossover transition CO(2,3) and the repump laser to the $F = 1 \rightarrow F' = 2$ transition. To extract information from an atomic cloud, we use an additional laser beam for absorption imaging [34]. We take time-of-flight (TOF) images with a probe beam pulse resonant with the $5^2S_{1/2}(F = 2) \rightarrow 5^2P_{3/2}(F = 3)$ transition, which casts a shadow on a CCD camera (Pco.pixelfly with 1392×1040 px²). To get a good signal the probe beam intensity must be below saturation which is for π -polarized

light $I_{\text{sat}} = 2.50 \text{ mW/cm}^2$ with the resonant cross section $\sigma = 1.9 \times 10^{-9} \text{ cm}^2$ [35].

The axially symmetric quadrupole field is generated by a pair of current carrying coils (mMOT coils) in anti-Helmholtz configuration. The mMOT coils are 45° -rotated with respect to the plane of the trap. The distance between the two coils is 27 cm and each coil consists of 36 windings of a hollow-core copper wire with a quadratic cross section (outer cross section $6 \times 6 \text{ mm}^2$ and an inner cross section $4 \times 4 \text{ mm}^2$) wrapped in Kapton tape for electrical insulation. These coils are internally cooled down to 20°C with a 300 Watts chiller (MINORE 0-RB400). At a maximum current of 200 A supplied by a high power source (SM 30-200 Delta Elektronika), we measure a magnetic field gradient of $\partial B^{\text{axial}}/\partial r_{\text{axial}} = 0.11 \text{ T/m}$ at the center of the trap which is at a few mm from the ion trap surface (Fig. 5). With a one winding coil behind the holder we can adjust the field, to push or pull the atom cloud in respect to the trap surface. For proper trapping efficiency measured magnetic field gradients are in the range of $0.10 - 0.20 \text{ T/m}$ [37].

Once atoms are captured in the mMOT, the mMOT coils will be switched to a bias field while switching on the big U-shaped wire beneath the atom chip which generates a quadrupole field with a minimum at infinity. The atoms can now be confined at about 2 mm underneath the chip surface in a spatially smaller area. The atoms will then be transferred to a potential created by the small U-shaped wire in the atom chip. At this step we shift the atoms close to the ion trap surface and compress the atom cloud to a smaller and steeper mMOT volume. As the final step we create an Ioffe-Pritchard trap by turning on the Z-shaped wire in the atom chip together with a bias magnetic field (Fig. 4). The axial direction of the atom cloud trapped in the magnetic field of the Z-shaped wire is not necessarily parallel to the z-axis of the ion trap. In the atom trap design we have considered the length of the Z-shaped wire to be 1.4 mm, so that the atom cloud overlaps with the ion cloud.

The ion trap we use in the experiment (Fig. 6) is a microfabricated surface trap with 21 DC electrodes which is fabricated in Translume technology [38,39]. A pulsed laser is used to pattern trenches of $50 \mu\text{m}$ deep and $10 \mu\text{m}$ wide in a fused silica substrate (SiO_2). Then material is etched with hydrofluoric acid which has a strong corrosive characteristic against SiO_2 . Finally the surface is coated with four metal layers of 20 nm Titanium, 150 nm gold, 20 nm Titanium and 150 nm gold, i.e. 300 nm gold in total. The high quality gold coating has a reflectance of about 90% for 780 nm light at an incident angle of 45° . According to successful operations of mMOTs on a microfabricated atom chip [40], and also on a magnetic lattice with periodicity of $10 \mu\text{m}$ [41], we expect a similar performance in our system.

The ion trap is glued on top of the atom trap using a UV adhesive (EPO-TEK[®] OG142-112 UV Cure Optical Epoxy). The adhesive is carefully applied at the edges of

the ion trap while preventing the adhesive to run between the two traps and is cured by illuminating it three times for 10 s with UV light. The electric connections between the ion trap and the filterboard are established by wire bonds ($25 \mu\text{m}$ diameter Pd wire). Planar Paul traps with characteristic length of about $100 \mu\text{m}$ have advantages in terms of fabrication and scalability [42,43,44,45,46,47,48]. In planar traps the ions are confined radially by RF potentials and axially by static electric voltages (DC) and all electrodes lie in a single plane [49]. There are several analytical approaches like a model by House [50] and Biot-Savart-like methods [51,52,53] to design planar traps with arbitrary geometries. In this report we use the House model for analytical determination of the applied DC and RF potentials to trap Yb^+ ions. The assembled trap is shown in Fig. 2 where the atom-ion chip is mounted upside-down on a carrier which is attached to a CF63 having various electrical feedthroughs. The chip surface is right in the middle of the vacuum chamber which guarantees optimal optical access [54]. Fig. 7 shows the complete vacuum setup and its main functional parts. Seven anti-reflection coated fused quartz silica viewports allow laser access to the center of the ion trap and the atom trap. The distance between the hybrid trap and the surface of the big window is 85 mm. To reach a UHV pressure, an ion getter pump (NEXTorr[®] D200-5) is attached to a cross right next to the chamber. The pressure we reach in our chamber is $1.3 \times 10^{-9} \text{ hPa}$.

3 Observation of ions We introduce our surface trap which has a F-shaped RF electrode for axial confinement of the ions. For the radial confinement it has 20 DC electrodes, which are placed axially symmetric around the RF rail and one compensation electrode in-between the legs of the RF. The optical resolution of our imaging system is about 720 nm and we typically trap Yb^+ ions at a distance of $150 \mu\text{m}$ to the surface of the trap and can position them axially with an accuracy of about $\pm 80 \text{ nm}$, see Sec. 4.

4 Ion trap operation The configuration of our Paul trap is linear, thus radial confinement is achieved by applying a RF sinusoidal drive field. Ions are confined in the node line of the quadrupole field that is generated from the electrodes. This harmonic binding in the radial r_1 and r_2 directions is described by a pseudopotential Φ_{RF} . Additionally, ions or ion crystals, are confined along the trap z axis by a DC harmonic oscillator potential Φ_{DC} . In the full description, both, RF and DC fields are independently adjusted for controlling the ion crystals' position and alignment, the inter-ion distances, and the trapping frequencies in all directions. The challenge is to find control voltages that suite the experimental protocol, and also match the condition that the center of the DC potential falls on the RF node line, where the ion micromotion is compensated (see Sec. 4.1).

The total effective potential for trapping the ions $\Phi(r, t)$ is given by the sum of a time-independent po-

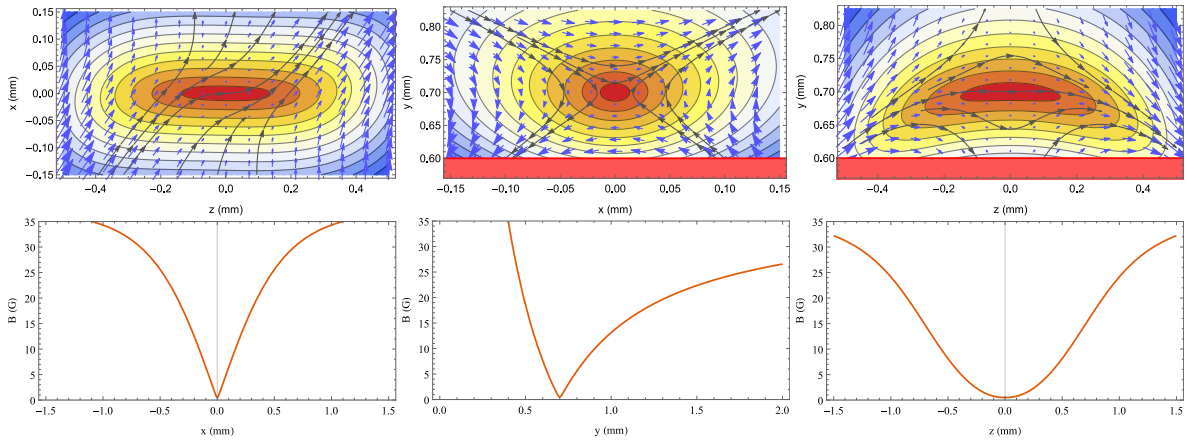


Figure 4 Potentials and B -fields of the Z-shaped wire in z - x , x - y and z - y planes with minimum at $x_0 = 0$ mm, $y_0 = 0.070$ mm and $z_0 = 0$ mm. Every color-step in the contour plots corresponds to 1 Gauss.

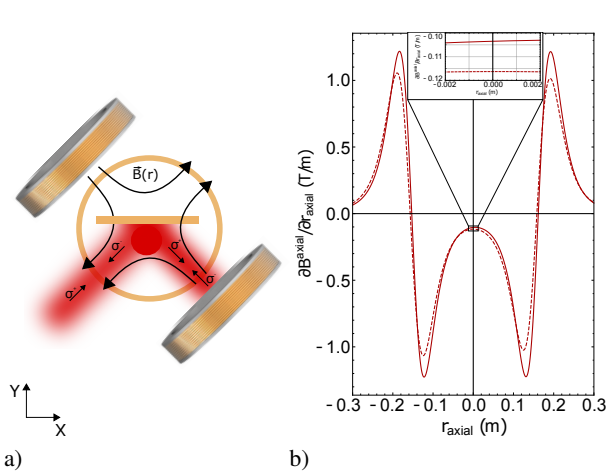


Figure 5 (a) The configuration of the laser beams and the quadrupole magnetic field to form a mMOT. (b) The magnetic field gradient along the axial direction of mMOT coils. The dashed line is the simulation using the Mathematica package Radia [36] and the solid line is the measurement.

tential Φ_{DC} generated by the trap DC electrodes and a sinusoidally varying part, the pseudopotential Φ_{RF} , that is driven by a RF voltage source:

$$\Phi(\mathbf{r}, t) = \Phi_{RF} + \Phi_{DC} \quad (4)$$

$$= \frac{q^2 V_{RF}^2}{4M\Omega_{RF}^2} \|\nabla\phi_{RF}\|^2 + Q \sum V_i \phi_{DC, i}, \quad (5)$$

here, q and M are the charge and mass of the trapped ions. V_{RF} and Ω_{RF} denote the RF amplitude and frequency, respectively. The potential terms ϕ_{RF} and ϕ_{DC} are the solution of the Laplace equation for a unit voltage applied to the RF and the i th DC electrode. V_i is the

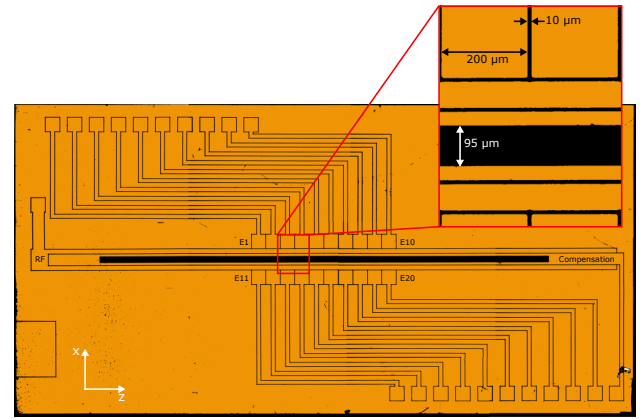


Figure 6 Optical microscope image of the microfabricated surface trap used in our experiment. The chip has a size of 9×4.5 mm² and a thickness of $500 \mu\text{m}$. It has a long and symmetric F-shaped rail for RF confinement, 20 static-voltage electrodes with a size of $200 \times 200 \mu\text{m}^2$ used for the radial confinement (E01 - E20) and one inner compensation electrode which is axially and symmetrically extending along a slit of $100 \mu\text{m}$ width and 5 mm length (E21). This slit is used to load Rb atoms from a dispenser placed right behind the ion trap. In the experiments described here, Yb^+ ion crystals are trapped and confined along the trap axis (z -direction). The gaps between the electrodes are approximately $10 \mu\text{m}$ wide and $50 \mu\text{m}$ deep, which are large enough that the RF voltage does not cause electrical breakdown at $100 - 200 V_{pp}$.

voltage applied on the i th DC electrode. The radial confinement of ions is realized by applying a RF voltage at a frequency of $\Omega_{RF} = 2\pi \times 11.22$ MHz and an amplitude of $109 V_{pp}$. This RF signal is generated by a RF generator (Rohde & Schwarz SML01), amplified (ZHL-5W-1-Mini Circuits) and sent to a helical resonator with a Q-factor of

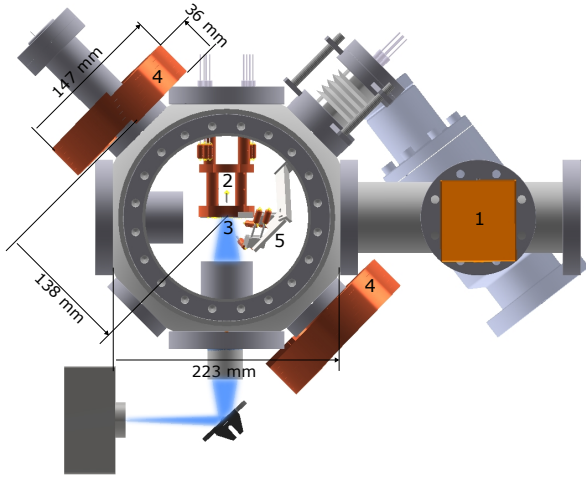


Figure 7 Overview of the system: 1. NEG pump, 2. Trap carrier with Rb atom source, 3. Hybrid trap, 4. mMOT coils, 5. Rb and Yb atom sources. The trap is mounted upside down on a home-made carrier which is attached to a special CF63 flange featuring various electrical feedthroughs. The trap surface is right in the middle of the vacuum chamber. Using a weld bellow (CF35/SEWB) one can adjust the atom sources relative to the trap chip.

360 to further enhance the signal [55]. With these values we reach a relatively small trap depth of 50 meV. In order to filter RF pickups, we have implemented a 3.38 MHz low-pass filter on the trap chip connected to each DC electrode and a second 50 kHz low-pass filter connected to the feedthrough. At our typical RF voltages we measured RF pickups of 116 – 930 mV_{pp} in the DC electrodes. Trapped ions are confined with typical trap frequencies of $(\omega_{r1}, \omega_{r2}, \omega_a) = 2\pi \times (485, 724, 289)$ kHz, where ω_a is the axial and ω_{r1} and ω_{r2} are the radial trap frequencies of the ion trap.

To provide the voltage for the DC electrodes, we use FPGA-controlled digital-to-analog conversion (DAC) boards. They allow sweeping voltages in real time and avoid delays caused by PCs. The ion transport is achieved by shifting the DC potential minimum. Therefore, ultra-fast voltage update rates need to be incorporated. This makes the use of FPGA controlled DACs necessary [56, 57]. Hence, the design we use is mainly comprised of a high-speed and low noise advance multichannel arbitrary waveform generator (N-MCWG) developed at the University of Mainz [58]. It supports up to 48 independent analog channels (16 bits) and 25 digital TTL signals per unit. Analog channels have a voltage range of -10 V to $+10$ V with a resolution of (0.12 mV 1 LSB).

The **Yb laser system** consists of three lasers used to ionize, cool and excite dipole transition of the Yb⁺ ions. For the initial steps we rely on ¹⁷⁴Yb⁺, while in the further run ¹⁷¹Yb⁺ with a long lived spin 1/2 system of

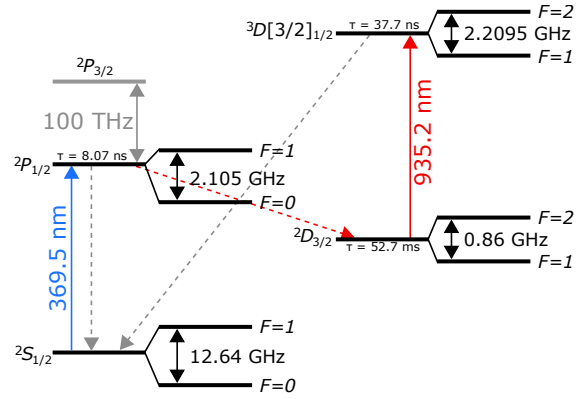


Figure 8 Energy level scheme of the electronic ground and excited states of ¹⁷¹Yb⁺ with nuclear spin $I=1/2$; the isotopes we have trapped are without nuclear spin. The transitions driven by diode lasers in our experiment are marked as straight lines. Life times and decay branching ratios are taken from [59]. Additional low-lying ²D_{5/2} and ²F_{7/2} states have been omitted for clarity.

ground states ²S_{1/2}($F = 0$) and ²S_{1/2}($F = 1$) will serve as qubit. The relevant level structure of ¹⁷¹Yb⁺ is shown in Fig. 8. To isotope-selectively ionize neutral Yb atoms, we use a two-step photoionization scheme [60]. First we excite the neutral Yb atoms from ¹S₀ → ¹P₀ with a home-made grating-stabilized diode laser at 398.9 nm (Nichia NDV4B16). The first step excitation is impinging the atomic beam under right angle and allows for isotope-selective excitation and trap loading [61, 62]. We use a Topica TA-SHG pro as a second step to the continuum and for cooling of ¹⁷⁴Yb⁺ ions, by exciting the ²S_{1/2} → ²P_{1/2} transition ($\Gamma = 2\pi \times 19.7$ MHz), which yields to laser-induced fluorescence for single ion detection at a wavelength of 369.5 nm. Ions in the ²P_{1/2} state can decay to the lower lying ²D_{3/2} state with a branching ratio of $\alpha = 0.00501(15)$ [63]. Therefore, to keep the ions in the cooling cycle, we use an additional Topica DL pro Laser at 935.2 nm to repump from the ²D_{3/2} → ³D[3/2]_{1/2} state ($\Gamma = 2\pi \times 4.2$ MHz). Both, the 369.5 nm and the 935.2 nm lasers are locked to Fabry-Pérot cavities with finesses of 630. The 369.5 nm cooling and the 398.9 nm photoionization lasers are coupled to the same polarization maintaining fiber and the outcome beam is overlapped with the 935 nm repump beam using a dichroic mirror. All beams pass through a $f = 125$ mm achromatic lens and are aligned in parallel to the surface of the trap. The beams have a slight angle of 7° to the trap axis. The cooling beam has an effective beam diameter of 30 μm at its focal point and a saturation power of about 60 μW. A magnetic field of 0.13 mT at 135° to the laser k-vector, sets the direction of the quantization axis. The fluorescence of the ions is collected with a microscope objective with a numerical aperture of 0.35 through an inverted viewport and detected by an EMCCD (Andor Luca 8 × 8 μm²) equipped with a

Table 2 Yb transition wavelengths (vacuum). These values are measured using a HighFinesse wavelength meter (WS6). The $^2S_{1/2} \rightarrow ^2P_{1/2}$ and $^2D_{3/2} \rightarrow ^3D[3/2]_{1/2}$ transition wavelengths were obtained by observing fluorescence signal levels from trapped ions.

Isotope	Ionization (nm)	Cooling (nm)	Repump (nm)
^{170}Yb	398.91070(5)	369.52360(5)	935.19750(5)
^{172}Yb	398.91100(5)	369.52440(5)	935.18730(5)
^{174}Yb	398.91135(5)	369.52495(5)	935.18015(5)
^{176}Yb	398.91160(5)	369.52550(5)	935.17240(5)

bandpass filter (FB370-10); Our imaging system has a calibration factor of $1.09(7) \mu\text{m}/\text{px}$ (Fig. 9).

The dark ion in Fig. 9 is in most of the times $^{172}\text{Yb}^+$ isotope. This isotope is the second most abundant isotope of Yb atom which has a photoionization energy close to the ^{174}Yb isotope. By trapping Yb^+ ions, we could find the cooling and repumping laser wavelengths for $^{170}\text{Yb}^+$, $^{172}\text{Yb}^+$, $^{174}\text{Yb}^+$ and $^{176}\text{Yb}^+$ which are all nuclear-spin free isotopes. The first step ionization wavelengths are extracted through the fluorescence signal of neutral Yb atoms (Tab. 2). These wavelengths are in good agreement with the values stated in Ref. [64].

We measured the lifetime of a single ion under continuous Doppler cooling and in the dark (Tab. 3). The lifetime of a Doppler cooled single ion is usually many hours but in our experiment we measured short lifetimes of 2 min only due to relatively high background gas pressure of 1.3×10^{-9} hPa. Nevertheless these values are in good agreement with other shallow surface Paul traps at room temperature [65]. The lifetime of a single ion in dark is about 1 min which is long enough for atom-ion interaction studies. In typical sequences, modifications of the loss rate are an observable at time scales of about 100 ms [66].

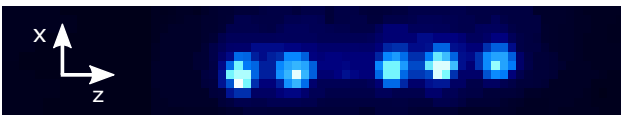


Figure 9 Linear crystal of $^{174}\text{Yb}^+$ ions trapped with corresponding trap frequencies of $(\omega_x, \omega_z) = 2\pi \times (406, 110)$ kHz. The dark ion observed is in most of the cases $^{172}\text{Yb}^+$. Each pixel in the image corresponds to $1.09(7) \mu\text{m}$.

Table 3 $1/e$ lifetimes (τ) of a single $^{174}\text{Yb}^+$ ion trapped in different axial positions of the trap.

Ion position	τ with cooling (s)	τ w/o cooling (s)
E02, E12	198.4 ± 0.5	50.5 ± 4.3
E04, E14	128.6 ± 0.8	40.6 ± 3.3
E06, E16	89.5 ± 0.5	39.9 ± 2.7
E08, E18	151.6 ± 0.6	31.7 ± 2.6

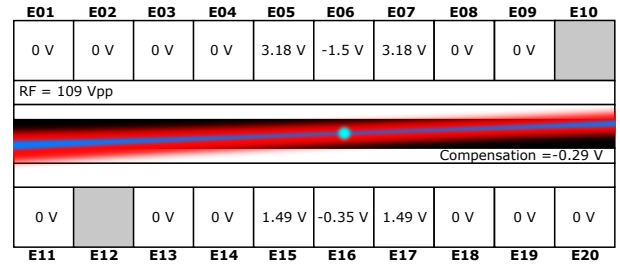


Figure 10 Simulated voltages to produce a tilted potential between electrodes E06 and E16 where the Yb^+ is trapped. The alignment of Gaussian beams are also schematically shown here.

In order to effectively cool the trapped ions, we need to tilt the principal axes of the ion so that a single laser can cool all three normal modes. All three Yb laser beams are aligned in parallel to the trap surface such that there is 12% projection of its k-vector on the radial trap axis (x and y) and resulting a negligible Doppler cooling efficiency in the radial directions. In order to tilt the principal axes of the ion, we apply DC voltages that are asymmetric along the x-axis (Fig. 10). These DC voltages are extracted following the analytic model for electrostatic fields in planar ion traps [50,67]. To create a non-harmonic potential we set the compensation electrode and one pair of opposing electrodes to different voltages and calculate the voltages for the surrounding electrodes to overlap the minimum of the DC and RF potentials. The tilted DC potential is shown in Fig. 11. Since we do not have control over each electrode, due to the shorts on the trap, we need to calculate special fields for electrical shorts to ground for some of the DC electrodes by neighboring electrodes. Note, that even with this constraint, the trap frequencies can be adjusted and measured values fit the theoretical expectation, see Fig. 12.

4.1 Micromotion compensation Micromotion compensation is an important and necessary condition for experiments where cold atoms interact with cold trapped ions. In cases, where the center of the DC potential and the RF potential are not superimposed the ions will undergo a fast oscillation at the frequency of the trap drive. This shift has to be determined and corrected by applying the proper corrections to the DC potential. For this, several methods have been applied [68,69,70] and the best compensation achieves a residual shift of $0.7 \mu\text{m}$ at respective trap frequencies of $(\omega_r, \omega_z) = 2\pi \times (350, 50)$ kHz [71]. We vary the RF amplitude and observe on the CCD image how the ion position is changing. In this way, we vary the DC control voltages such that the ion position does no longer change with the variation of the RF amplitude, see Fig. 13

A systematic measurement of the stray electric fields is done analogues to Ref. [68]. As an example we measure for the case when the ion is over electrodes E06 and E16. We set the surrounding voltages to the simulated set of voltages

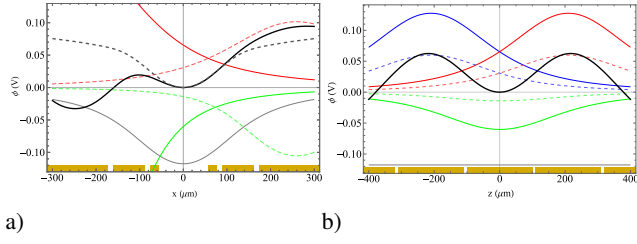


Figure 11 DC potential along x - and z -axis of the ion trap. (a) The black dotted line is a DC potential without tilting, while the solid black line is the tilted DC potential created by neighboring DC potentials shown in different colors. (b) Tilted DC potential along the axis of the ion trap. The middle DC electrodes are E06 and E16.

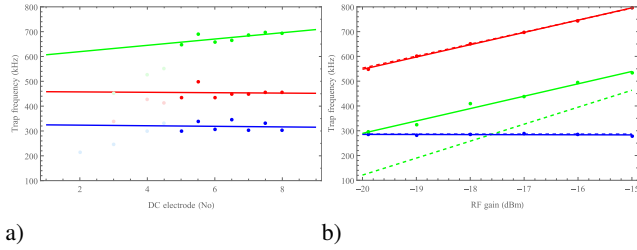


Figure 12 (a) Trap frequencies along the axis of the ion trap, light dots mark the frequencies for special potentials. (b) Trap frequencies with respect to the applied RF gain. Blue: axial frequency, Green and Red: radial frequencies. Dotted lines are the simulated and solid lines the measured values. The differences result from the tilted axes, which are not taken into account for the calculation of the radial frequencies.

shown in Fig. 10. The experimental procedure is to vary the RF gain between -20 and -15 dBm shown at the RF generator and measure the corresponding position of the ion. In each of the following steps we change the voltage of one of the surrounding DCs and repeat the RF variation and position determination. This measurement leads to a 2D plot, where the ion position is always moving towards the RF null for high RF amplitudes. If the compensation is improved there will be less displacement by varying the RF power. One can see, that the simulated values are not optimized. As a conclusion we have to adjust the voltage of electrode E06 to -1.0 V to achieve the best compensation. The electrodes sitting right below the ion are important for compensation, while the rest of electrodes are used to shift the position of the ion along the RF node. The residual stray electric field $\varepsilon_{\text{stray}}$ can shift the ion position away from the RF node to position

$$\mathbf{r}_\varepsilon \approx \frac{q}{m} \sum_k \frac{\varepsilon_{\text{stray},k}}{\omega_k^2} \hat{\mathbf{k}}, \quad (6)$$

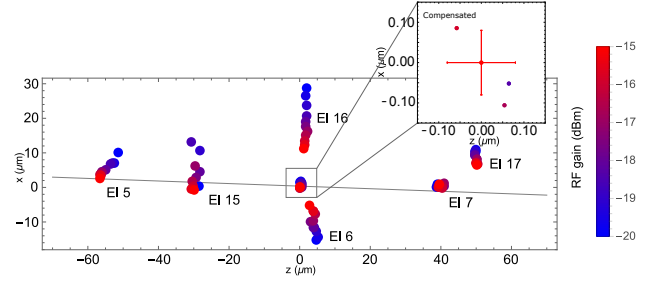


Figure 13 Residual stray electric fields after the micromotion compensation. Each dot is showing the position of a single ion at different RF gains. Each group of data is taken with the same set of DC voltages listed in Fig. 10 but varied RF gains. The gray line represents the trap axis, extrapolated from the compensated positions over each pair of electrodes. The error bar is the standard error of the Gaussian fit to a single ion image. Voltages used for the micromotion compensation are E05: 0.68 V, E06: -4.5 V, E07: 0.68 V, E15: -0.01 V, E16: -3.35 V and E17: -0.51 V. The optimized voltage is -1.0 V applied to E06.

where \mathbf{r}_ε is the average position of the ion in $\hat{\mathbf{k}} = (x, y, z)$ direction, q the charge of the ion, m the mass of the ion and ω_k the secular frequencies. We can measure the \mathbf{r}_ε from a single ion image and therefore extract the residual stray electric field $\varepsilon_{\text{stray}}$. After the 2D compensation we estimate a residual electric stray field uncertainty of $(\Delta\varepsilon_{\text{stray},x}, \Delta\varepsilon_{\text{stray},z}) = (0.90, 0.30)$ V/m with the corresponding trap frequencies of $(\omega_z, \omega_x) = 2\pi \times (305, 435)$ kHz. The residual electric stray field uncertainty measured in our ion trap are sufficient enough for a first atom-ion interaction study but in the future we will extend the 2D micromotion compensation to a full 3D by using parametric resonance excitation induced by potential modulation [69].

5 Conclusion and outlook We have introduced a hybrid atom-ion experimental setup to trap the Yb^+ ions and the ^{87}Rb atoms to investigate atom-ion interaction. Our setup is a compact planar Paul trap with segmented DC electrodes, featuring the exact positioning of single ions. We characterized the trap performance including minimization of micromotion arising from stray electric fields. Comparing the residual electric stray fields to literature the micromotion compensation should be good enough for atom-ion interactions. Controlled movement of the ions in the axial direction of the trap for about 1.6 mm is also accomplished. The next step in our experiment will be trapping ^{87}Rb atoms before we overlap them with the ion crystals in order to investigate atom-ion collision dynamics.

Acknowledgements This work was supported by the EU-STREP EQuaM and the SFB/TR49. We thank Johannes Denschlag (Univ. of Ulm), Hartmut Häffner (Univ. of California

Berkeley) for support and Arezoo Mokhberi for helpful discussions. A. Bahrami and M. Müller contributed equally to this work.

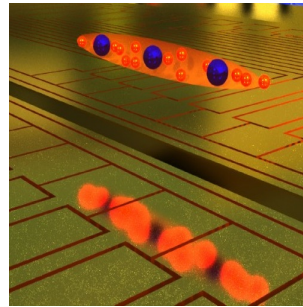
References

- [1] F. Dalfovo, S. Giorgini, L. P. Pitaevskii, and S. Stringari, *Rev. Mod. Phys.* **71**, 463 (1999).
- [2] S. Giorgini, L. P. Pitaevskii, and S. Stringari, *Rev. Mod. Phys.* **80**, 1215 (2008).
- [3] M. Greiner, C. A. Regal, and D. S. Jin, *Nature* **426**, 537 (2003).
- [4] C. A. Regal, M. Greiner, and D. S. Jin, *Phys. Rev. Lett.* **92**, 040403 (2004).
- [5] D. Leibfried, R. Blatt, C. Monroe, and D. Wineland, *Rev. Mod. Phys.* **75**, 281 (2003).
- [6] F. H. J. Hall, M. Aymar, N. Bouloufa-Maafa, O. Dulieu, and S. Willitsch, *Phys. Rev. Lett.* **107**, 243202 (2011).
- [7] W. G. Rellergert, S. T. Sullivan, S. Kotochigova, A. Petrov, K. Chen, S. J. Schowalter, and E. R. Hudson, *Phys. Rev. Lett.* **107**, 243201 (2011).
- [8] L. Ratschbacher, C. Zipkes, C. Sias, and M. Köhl, *Nat. Phys.* **8**, 649 (2012).
- [9] R. Côté, V. Kharchenko, and M. D. Lukin, *Phys. Rev. Lett.* **89**, 093001 (2002).
- [10] U. Bissbort, D. Cocks, A. Negretti, Z. Idziaszek, T. Calarco, F. Schmidt-Kaler, W. Hofstetter, and R. Gerritsma, *Phys. Rev. Lett.* **111**, 080501 (2013).
- [11] R. Côté, *Phys. Rev. Lett.* **85**, 5316 (2000).
- [12] G. F. Gribakin and V. V. Flambaum, *Phys. Rev. A* **48**, 546 (1993).
- [13] T. M. Miller and B. Bederson, *CRC Handbook of Chemistry and Physics*, Edited by David R. Lide (1989).
- [14] C. Chin, R. Grimm, P. Julienne, and E. Tiesinga, *Rev. Mod. Phys.* **82**, 1225 (2010).
- [15] R. Côté and A. Dalgarno, *Phys. Rev. A* **62**, 012709 (2000).
- [16] O. P. Makarov, R. Côté, H. Michels, and W. W. Smith, *Phys. Rev. A* **67**, 012709 (2003).
- [17] B. J. Verhaar, J. M. V. A. Koelman, H. T. C. Stoof, O. J. Luiten, and S. B. Crampton, *Phys. Rev. A* **35**, 3825 (1987).
- [18] D. L. Cooper, K. Kirby, and A. Dalgarno, *Can. J. Phys.* **62**, 1622 (1984).
- [19] B. Zygelman and A. Dalgarno, *Phys. Rev. A* **38**, 1877 (1988).
- [20] B. Zygelman, A. Dalgarno, M. Kimura, and N. F. Lane, *Phys. Rev. A* **40**, 2340 (1989).
- [21] A. Rakshit and B. Deb, *Phys. Rev. A* **83**, 76 (2011).
- [22] R. Gerritsma, A. Negretti, H. Doerk, Z. Idziaszek, T. Calarco, and F. Schmidt-Kaler, *Phys. Rev. Lett.* **109**, 080402 (2012).
- [23] M. Albiez, R. Gati, J. Fölling, S. Hunsmann, M. Cristiani, and M. K. Oberthaler, *Phys. Rev. Lett.* **95**, 010402 (2005).
- [24] B. Höltkemeier, P. Weckesser, H. Lpez-Carrera, and M. Weidemüller, *Phys. Rev. Lett.* **116**, 233003 (2016).
- [25] Z. Idziaszek, T. Calarco, and P. Zoller, *Phys. Rev. A* **76** (2007).
- [26] J. Goold, H. Doerk, Z. Idziaszek, T. Calarco, and T. Busch, *Phys. Rev. A* **81** (2010).
- [27] M. Cetina, A. T. Grier, and V. Vuletić, *Phys. Rev. Lett.* **109**, 253201 (2012).
- [28] C. Zipkes, S. Palzer, L. Ratschbacher, C. Sias, and M. Köhl, *Phys. Rev. Lett.* **105**, 133201 (2010).
- [29] G. Audi, O. Bersillon, J. Blachot, and A. H. Wapstra, *Nucl. Phys. A* **729**, 3–128 (2003).
- [30] P. A. Ivanov, N. V. Vitanov, and K. Singer, *Sci. Rep* **6**, 28078 (2016).
- [31] N. Nemitz, F. Baumer, F. Mchow, S. Tassy, and A. Görlitz, *Phys. Rev. A* **79**, 061403(R) (2009).
- [32] F. Schmidt-Kaler and R. Gerritsma, *EPL* **99**, 53001 (2012).
- [33] J. Reichel, W. Hänsel, and T. W. Hänsch, *Phys. Rev. Lett.* **83**, 3398 (1999).
- [34] M. O. Mewes, M. R. Andrews, N. J. van Druten, D. M. Kurn, D. S. Durfee, and W. Ketterle, *Phys. Rev. Lett.* **77**, 416 (1996).
- [35] D. A. Steck, "Rubidium 87 D line data", available online at <http://steck.us/alkalidata>, **2.1.5** (2015).
- [36] P. Elleaume, O. Chubar, and J. Chavanne, *proc. of the PAC97 Conference May 1997* pp. 3509–3511 (1997).
- [37] S. Wildermuth, P. Krüger, C. Becker, M. Brajdic, S. Haupt, A. Kasper, R. Folman, and J. Schmiedmayer, *Phys. Rev. A* **69**, 030901 (2004).
- [38] N. Daniilidis, S. Gerber, G. Bolloten, M. Ramm, A. Ransford, E. Ulin-Avila, I. Talukdar, and H. Häffner, *Phys. Rev. B* **89**, 0901 (2014).
- [39] A. Bautista-Salvador, PhD thesis, Ulm University (2015).
- [40] R. Folman, P. Krüger, D. Cassettari, B. Hessmo, T. Maier, and J. Schmiedmayer, *Phys. Rev. Lett.* **84**, 4749 (2000).
- [41] S. Jose, P. Surendran, Y. Wang, I. Herrera, L. Krzemien, S. Whitlock, R. McLean, A. Sidorov, and P. Hannaford, *Phys. Rev. A* **89**(May), 051602 (2014).
- [42] D. Kielpinski, C. Monroe, and D. J. Wineland, *Nature* **417**, 709 (2002).
- [43] M. J. Madsen, W. K. Hensinger, D. Stick, J. A. Rabchuk, and C. Monroe, *Appl. Phys. B: Lasers and Optics* **78**, 639 (2004).
- [44] S. Seidelin, J. Chiaverini, R. Reichle, J. J. Bollinger, D. Leibfried, J. Britton, J. H. Wesenberg, R. B. Blakestad, R. J. Epstein, D. B. Hume, W. M. Itano, J. D. Jost, C. Langer, R. Ozeri, N. Shiga, and D. J. Wineland, *Physica Rev. Lett.* **96**, 253003 (2006).
- [45] C. E. Pearson, D. R. Leibbrandt, W. S. Bakr, W. J. Mallard, K. R. Brown, and I. L. Chuang, *Phys. Rev. A* **73**, 259 (2006).
- [46] D. R. Leibbrandt, R. J. Clark, J. Labaziewicz, P. Antohi, W. Bakr, K. R. Brown, and I. L. Chuang, *Phys. Rev. A* **76**, 515 (2007).
- [47] S. X. Wang, J. Labaziewicz, Y. Ge, R. Shewmon, and I. L. Chuang, *Appl. Phys. Lett.* **94**, 094103 (2009).
- [48] J. M. Amini, J. Britton, D. Leibfried, and D. J. Wineland, *Microfabricated chip traps for ions*, Wiley-VCH, Weinheim, Germany (2011).
- [49] J. Chiaverini, R. B. Blakestad, J. Britton, J. D. Jost, C. Langer, D. Leibfried, R. Ozeri, and D. J. Wineland, *Quantum Information and Computation* **5**, 419 (2005).
- [50] M. G. House, *Phys. Rev. A* **78**, 419 (2008).
- [51] M. H. Oliveira and J. A. Miranda, *Eur. J. Phys.* **22**, 31 (2001).
- [52] J. H. Wesenberg, *Phys. Rev. A* **78**, 419 (2008).
- [53] R. Schmied, *New J. Phys.* **12**, 023038 (2010).

- [54] J. Joger, Diploma Thesis, Johannes-Gutenberg University Mainz, Germany, 2013.
- [55] J.D. Siverns, L.R. Simkins, S. Weidt, and W.K. Hensinger, *Appl. Phys. B: Lasers and Optics* **107**, 921 (2012).
- [56] A. Walther, F. Ziesel, T. Ruster, S.T. Dawkins, K. Ott, M. Hettrich, K. Singer, F. Schmidt-Kaler, and U. Poschinger, *Phys. Rev. Lett.* **109**, 080501 (2012).
- [57] T. Ruster, C. Warschburger, H. Kaufmann, C.T. Schmiegelow, A. Walther, M. Hettrich, A. Pfister, V. Kaushal, F. Schmidt-Kaler, and U.G. Poschinger, *Phys. Rev. A* **90**, 033410 (2014).
- [58] F. Schmidt-Kaler, Quantenbit AG Schmidt-Kaler.
- [59] S.M. Olmschenk, D.N. Matsukevich, P. Maunz, D.F. Hayes, Duan L. M., and C. Monroe, *Science*, 486 (2009).
- [60] M. Aymar, A. Debarre, and O. Robaux, *J. Phys. B: Atomic and Molecular Physics* **13**, 1089 (1980).
- [61] S. Gulde, D. Rotter, P. Barton, F. Schmidt-Kaler, R. Blatt, and W. Hogervorst, *Appl. Phys. B* **73**, 861–863 (2001).
- [62] M. Johanning, A. Braun, D. Eiteneuer, C. Paape, C. Balzer, W. Neuhauser, and C. Wunderlich, *Appl. Phys. B* **103**, 327–338 (2011).
- [63] S. Olmschenk, K.C. Younge, D.L. Moehring, D.N. Matsukevich, P. Maunz, and C. Monroe, *Phys. Rev. A* **76**, 259 (2007).
- [64] J.J. McLoughlin, A.H. Nizamani, J.D. Siverns, R.C. Sterling, M.D. Hughes, B. Lekitsch, B. Stein, S. Weidt, and W.K. Hensinger, *Phys. Rev. A* **83**, 259 (2011).
- [65] D.R. Leibbrandt, J. Labaziewicz, R. Clark, I.L. Chuang, R.J. Epstein, C. Ospelkaus, J.H. Wesenberg, J.J. Bollinger, D. Leibfried, D. Wineland, D. Stick, J. Sterk, C. Monroe, C.S. Pai, Y. Low, R. Frahm, and R.E. Slusher, *Quantum Information and Computation* **9**, 901 (2009).
- [66] J. Joger, H. Fürst, N. Ewald, T. Feldker, M. Tomza, and R. Gerritsma, *Phys. Rev. A* **96**, 030703 (2017).
- [67] D.T.C. Allcock, J.A. Sherman, D.N. Stacey, A.H. Burrell, M.J. Curtis, G. Imreh, N.M. Linke, D.J. Szwer, S.C. Webster, A.M. Steane, and D.M. Lucas, *New J. Phys* **12**, 053026 (2010).
- [68] T.F. Gloger, P. Kaufmann, D. Kaufmann, M.T. Baig, T. Collath, M. Johanning, and C. Wunderlich, *Phys. Rev. A* **92**, 043421 (2015).
- [69] Y. Ibaraki, U. Tanaka, and S. Urabe, *Appl. Phys. B* **105**, 219–223 (2011).
- [70] D.J. Berkeland, J.D. Miller, J.C. Bergquist, W.M. Itano, and D.J. Wineland, *J. Appl. Phys.* **83**, 5025 (1998).
- [71] A. Härter, A. Krüchow, A. Brunnera, and J.H. Denschlag, *Appl. Phys. Lett.* **102**, 221115 (2013).

Graphical Table of Contents

GTOC image:



We introduce a new micro-fabricated planar ion trap combined with an integrated atom trap into a single chip. Trapped single ions can be coupled to a small neutral atom cloud enabling us to investigate atom-ion interactions. This includes the tunneling dynamics of a bosonic Josephson junction and spin dynamics of ions inside polarized neutral atoms.